High-Field Transport and Thermal Reliability of Sorted Carbon Nanotube Network Devices

Ashkan Behnam,[†,‡,*] Vinod K. Sangwan,[§] Xuanyu Zhong,[‡] Feifei Lian,[†,‡] David Estrada,[†,‡] Deep Jariwala,[§] Alicia J. Hoag,[‡] Lincoln J. Lauhon,[§] Tobin J. Marks,[§,⊥] Mark C. Hersam,[§,⊥] and Eric Pop[†,‡,¶,*]

[†]Micro and Nanotechnology Laboratory, [‡]Department of Electrical and Computer Engineering, and [¶]Beckman Institute, University of Illinois at Urbana, Champaign, Illinois 61801, United States and [§]Department of Materials Science and Engineering and [⊥]Department of Chemistry, Northwestern University, Evanston, Illinois 60208, United States

ABSTRACT We examine the high-field operation, power dissipation, and thermal reliability of sorted carbon nanotube network (CNN) devices, with <1% to >99% semiconducting nanotubes. We combine systematic electrical measurements with infrared (IR) thermal imaging and detailed Monte Carlo simulations to study high-field transport up to CNN failure by unzipping-like breakdown. We find that metallic CNNs carry peak current densities up to an order of magnitude greater than semiconducting CNNs at comparable nanotube densities. Metallic CNNs also appear to have a factor of 2 lower intrinsic thermal resistance, suggesting a lower thermal resistance at metallic nanotube junctions. The performance limits and reliability of CNNs depend on their makeup, and could be improved by carefully engineered heat dissipation through the substrate, contacts, and nanotube junctions. These results are essential for optimization of CNN devices on transparent or flexible substrates which typically have very low thermal conductivity.

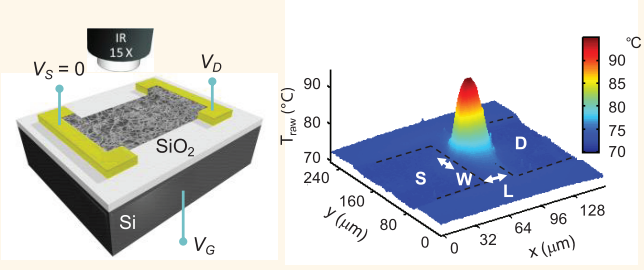

KEYWORDS: carbon nanotube · network · electrical breakdown · thermal conductivity · power dissipation · nanotube junctions · ultracentrifugation · infrared microscopy · percolation

Individual single-walled carbon nanotubes (SWCNTs) have excellent intrinsic properties such as high electron and hole mobility ($\mu \approx 10^4$ cm^2 V^{-1} s^{-1}) and high thermal conductivity ($\kappa \approx 3000$ W m^{-1} K^{-1}).[1,2] However, values of μ (<200 cm^2 V^{-1} s^{-1}) and κ (<100 W m^{-1} K^{-1}) are significantly reduced when SWCNTs are coupled with each other to form carbon nanotube networks (CNNs).[3−6] The degradation in material performance is mainly due to the large electrical[7−11] and thermal[12−16] junction resistances between SWCNTs or their bundles. Junction resistances vary significantly with parameters such as diameter and orientation of the SWCNTs[9,12,16] and in particular the electrical junction resistance is a strong function of the SWCNT electronic type (semiconducting or metallic).[10,17] Nevertheless, recent developments in large-scale and low-temperature fabrication techniques with control over bundle density, length, and type[18−23] make CNNs suitable for applications such as sensors, interconnects, and flexible electronics where they can outperform amorphous silicon and organic transistors.[23−25]

For CNNs to find wider use in these emerging applications, a better understanding of their performance and reliability are critical. Some reports have analyzed the low-field performance of CNNs and reported the dependence of transport properties such as ON/OFF ratio and mobility on SWCNT density and electric type.[3,26] However, only a few studies have investigated high-field reliability of CNN-based devices[27−29] due to the complexity and heterogeneity of such networks. In addition, no studies have focused on the combined effects of important parameters such as CNN morphology and SWCNT electronic type[20−22] on high-field device properties and performance limits during practical operating conditions. There is also a need to develop electrical and thermal computational models of CNNs in order to analyze effects of various network parameters, optimize device designs, and gain fundamental insights into their operation.

* Address correspondence to abehnam@illinois.edu, epop@illinois.edu.

Received for review October 3, 2012 and accepted December 6, 2012.

Published online December 24, 2012
10.1021/nn304570u

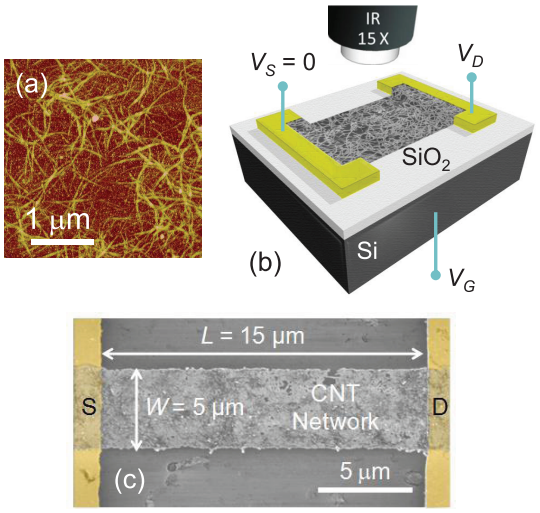

Figure 1. (a) Atomic force microscope (AFM) image showing the morphology of a typical carbon nanotube network (CNN). Individual SWCNT diameters in this work fall mostly between 1.4 and 1.6 nm (Supporting Information, Figure S6), although SWCNTs within CNN devices are often bundled (Supporting Information, Figure S7). (b) Schematic of the device structure and measurement setup, including applied biases and microscope lens for simultaneous thermal infrared (IR) imaging. (c) Scanning electron microscope (SEM) image showing CNN device structure and dimensions; source (S) and drain (D) contacts are colorized for clarity. Various devices with $L = 2-150$ μm and $W = 5-150$ μm have been fabricated (see Methods).

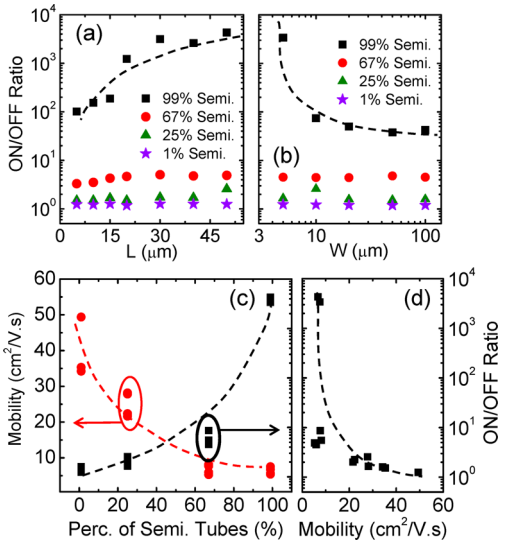

Figure 2. (a) ON/OFF ratio *vs* L for CNNs with $W = 5$ μm and various percentages of semiconducting SWCNTs. (b) ON/OFF ratio *vs* W for CNNs with $L = 40$ μm and various percentages of semiconducting SWCNTs. (c) Mobility, μ, and ON/OFF ratio *vs* percentage of semiconducting SWCNTs in CNNs. $L = 40$ or 50 μm and $W = 5$ μm. (d) ON/OFF ratio *vs* μ for devices shown in panel c. Dashed lines are guides to the eye.

In this study, we bring together comprehensive experimental characterization and computational modeling to better understand high-field transport, thermal dissipation, and breakdown phenomena in CNN thin film transistors (TFTs). Experimentally, we find that field-effect mobility (μ), current ON/OFF ratio, and breakdown parameters in the fabricated devices depend strongly on the percentage of semiconducting SWCNTs in CNNs. Surprisingly, however, high-field properties such as maximum current and power densities, as well as breakdown voltage do not strongly depend on gating voltage regardless of the semiconducting SWCNT fraction within the CNN. In parallel with electrical characterization, we use infrared (IR) thermal imaging to analyze power dissipation and temperature distribution in CNNs.[27] The results show that overall thermal resistances of metallic CNNs (m-CNNs) are lower than those of semiconducting CNNs (s-CNNs). We also construct a Monte Carlo computational model of such CNNs that captures the dynamics of the network heating process and predicts reliability results in agreement with experimental observations. Such models also facilitate analysis of the effects on device performance of CNN parameters that are experimentally difficult to probe directly (*e.g.*, SWCNT junctions).

RESULTS AND DISCUSSION

Low-Field Transport in CNNs. Figure 1a shows a typical atomic force microscope (AFM) image of the CNN morphology in one of the fabricated CNN devices (see Methods section for fabrication details). Optical absorbance, Raman spectroscopy, and AFM imaging techniques are used to characterize the percentage of semiconducting SWCNTs, their density, and diameters in fabricated CNNs (Supporting Information Figures S1–S7). Figure 1 panels b and c illustrate the device measurement setup and a scanning electron microscope (SEM) image of a CNN-TFT, respectively. We use a 3-terminal measurement setup (with a back gate voltage applied to the highly doped Si substrate) to characterize devices electrically, and an IR thermal microscope to simultaneously characterize them thermally.

We find that low-field transport in CNN devices depends strongly on device dimensions and fraction of semiconducting SWCNTs.[20,23] All types of devices show p-type doping (Supporting Information, Figure S8a). As expected, for devices with substantial percentages of metallic SWCNTs the ON/OFF ratio [I_D ($V_G = -30$ V)/I_D ($V_G = +30$ V)] is quite low (<10) and also a weak function of the device length (L) or width (W) (Figure 2a,b and Supporting Information, Figure S8a,b). However, for s-CNNs with >99% semiconducting SWCNTs the ON/OFF ratio is not only higher than in other CNNs,[22] but it also increases significantly as L is increased (Figure 2a) or W is reduced (Figure 2b). With an increase in L or decrease in W, the probability of having shorted metallic paths between the two device terminals is reduced. At the same time, the number of semiconducting tube segments in each current path is increased, resulting in an overall increase in gate control over the number of carriers in the channel. ON/OFF ratio scaling with L is stronger for $L < 20$ μm

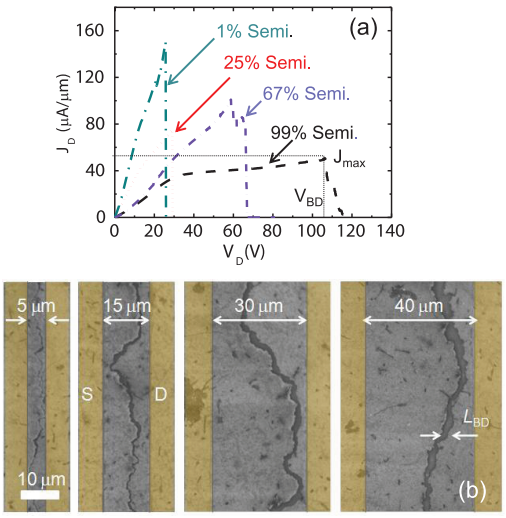

Figure 3. (a) Current density per width J_D *vs* V_D up to breakdown for devices with various percentages of semiconducting SWCNTs. $L = 10\ \mu m$, $W = 50\ \mu m$, $V_G = -30$ V (ON state). Breakdown voltage (V_{BD}) and maximum current density (J_{max}) points are shown for one of the curves. (b) Series of scanning electron microscope (SEM) images of CNN devices (67% semiconducting) with various lengths after electrical breakdown in the ON state. In all cases a random but zigzag breakdown path forms across the width of devices. The increase in the length of the breakdown gap (L_{BD}) with an increase in L is noticeable. Source (S) and drain (D) terminals colorized for emphasis.

but tends to eventually saturate for $L > 40\ \mu m$ when the gate control over the network is already very strong. The ON/OFF ratio is almost constant for $W > 10\ \mu m$, but increases dramatically for $W < 10\ \mu m$ (at large L) when transport is limited to paths of several SWCNTs in series (no fully metallic paths).[24,25,30]

The field-effect mobility, μ, calculated from the average slope of forward and reverse current−gate voltage sweeps,[21] is also a strong function of semiconducting SWCNT percentage in CNNs. Unlike the ON/OFF ratio, μ decreases (by up to 5×) as the percentage of semiconducting tubes is increased (Figure 2c and Supporting Information, Figure S8c). The inverse relationship between the ON/OFF ratio and μ is shown in Figure 2d and Supporting Information, Figure S8d, in agreement with existing literature on CNN devices.[31,32] On the basis of the above results, using s-CNNs with high ON/OFF ratios (*e.g.*, > 1000×) would be necessary for large-scale TFT applications, while m-CNNs are more desirable for applications where only high transparency and good CNN conductivity are important (see sheet resistance values in Supporting Information, Figure S8e). In addition, low-field contact resistance between m-CNNs and metal electrodes (as estimated from a transmission line analysis on CNN devices with various lengths[33]) is lower compared to other types of CNNs, which is important for power consumption minimization in any device design (Figure S8e).

High-Field Transport and Thermal Breakdown of CNNs. Figure 3a shows several examples of high-field current flow in the present CNNs, up to device breakdown in the ON mode ($V_G = -30$ V). These CNNs have identical dimensions, but contain various percentages of semiconducting tubes. The current (I_D) and current density (J_D) in m-CNNs increase almost linearly as the drain voltage (V_D) is increased. Eventually, m-CNNs break down sharply at relatively lower drain voltages (V_D = 10−30 V for $L = 10\ \mu m$) while tolerating large maximum current densities ($J_{max} > 100\ \mu A/\mu m$). We take V_D at maximum power density as the breakdown voltage, V_{BD}. With an increase in the percentage of semiconducting tubes in the CNN, V_{BD} increases and the maximum current density (J_{max}) decreases. Unlike m-CNNs, s-CNNs show clear current saturation at high voltages. As shown in Figure 3b and Supporting Information, Figure S9a, CNN breakdown results in a continuous zigzag gap across the width of the network regardless of CNN dimensions investigated here (Figure 3b and Supporting Information, Figure S9a). However, for nonuniform or mixed CNNs, occasionally there are small drops in current before the final breakdown point (see CNN with 67% semiconducting SWCNT in Figure 3a). For such CNNs it may be possible to intentionally induce partial breakdowns (Supporting Information, Figure S9b), a technique that has been used to selectively remove metallic nanotubes and improve ON/OFF ratios in sparse CNNs.[34,35] However, in dense CNNs (like those presented here) all types of SWCNTs appear to break down together, in a process that is assisted by source/drain induced electric field and is independent of the gate bias. These features, which will be discussed below, would make the additional postsynthesis sorting process less efficient.

The breakdown voltage V_{BD} is a strong function not only of semiconducting SWCNT percentage in CNNs, but also of other CNN parameters such as device length. Figure 4a shows that $V_{BD,net}$ (portion of V_{BD} that is dropped across the CNN and not the metal electrodes) scales almost linearly with L for all cases, but the slope of the linear fit (effective breakdown field) increases significantly with the percentage of the semiconducting SWCNTs. Since the electrical junction resistance between two metallic SWCNTs is significantly lower than that of other types of junctions,[10,11,36] m-CNNs have lower sheet resistances compared to other CNNs (Supporting Information, Figure S8e). As a result, smaller voltages are needed to initiate the breakdown in m-CNNs.

Scaling of device length has other interesting effects on breakdown in CNNs, for instance the average length of the breakdown gap (L_{BD}) increases significantly with L (Figure 3b). In sufficiently dense CNNs, the breakdown initiates at a local hot spot and immediately leads to an increased voltage drop across this partly burned region. Thus, the increased local electric field and temperature assist in triggering breakdown of neighboring SWCNTs, creating the "unzipped" gap across the device width.[28] The higher V_{BD} applied to long CNNs results in larger electric fields across the

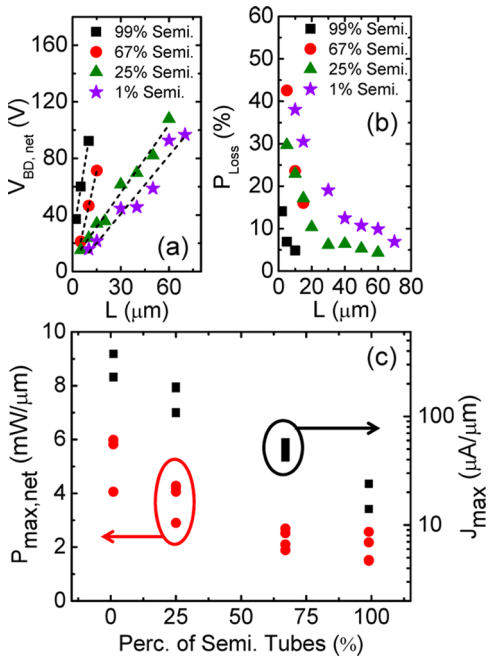

Figure 4. (a) Net breakdown voltage $V_{BD,net}$ in the ON state *vs* device length *L*, at $W = 100\ \mu$m. The slopes of the dashed lines represent average electric fields at breakdown, 6.85, 5, 1.6, and 1.35 V/μm for 99%, 67%, 25%, and 1% semiconducting CNNs, respectively. (b) Percentage of breakdown power dissipated over the contacts P_{loss} *vs* *L* for various percentages of semiconducting SWCNTs, symbols consistent with those in panel a. (c) Normalized maximum power (P_{max}) and J_{max} *vs* percentage of semiconducting SWCNTs. $L = 10\ \mu$m and $W = 100\ \mu$m.

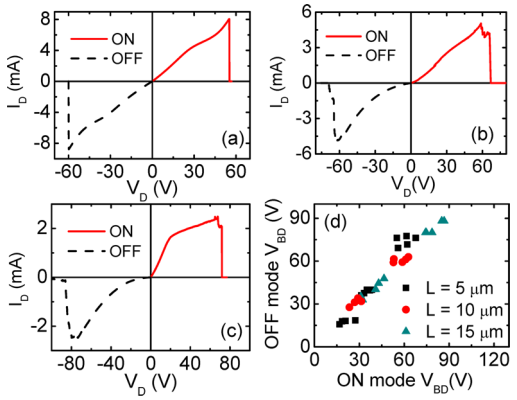

Figure 5. Dependence of CNN I_D-V_D characteristics up to breakdown on V_G and the percentage of semiconducting SWCNTs. ON and OFF measurements are performed at $V_G = -30$ and $+30$ V, respectively. (a) Metallic CNN with $L = 30\ \mu$m and $W = 20\ \mu$m. (b) 33% metallic CNN with $L = 10\ \mu$m and $W = 100\ \mu$m. (c) Semiconducting CNN with $L = 5\ \mu$m and $W = 100\ \mu$m. (d) Relationship between V_{BD} in ON and OFF modes for various CNNs showing nearly identical breakdown voltages in the ON and OFF states (see text).

broken regions and therefore formation of larger breakdown gaps. In addition, longer CNNs have a more uniform, "flatter" temperature distribution. Therefore, more hot spots can form in the channel and merge together to form larger gaps during breakdown.

A portion of the applied V_{BD} drops across metal electrodes and the metal-CNN contacts, leading to some power loss at the contacts (P_{Loss}, calculated as a percentage of the total power, equal to total contact resistance divided by the device resistance). P_{Loss} increases significantly as *L* decreases for all types of CNNs, reaching 30−40% for short low-resistance devices (Figure 4b). These confirm that contact engineering should play a significant role in minimizing higher power dissipation in scaled CNNs. The rest of the breakdown power ($P_{max,net}$, normalized to *W*) is generated intrinsically by the CNN. Both $P_{max,net}$ and J_{max} (Figure 4c) increase with a reduction in the percentage of semiconducting SWCNTs in the CNN, such that m-CNNs can tolerate ~10× higher current density and ~3× higher power density compared to s-CNNs. The increase in J_{max} for m-CNNs is partially due to the lower sheet and contact resistance of m-CNNs. The increase in $P_{max,net}$ is related to the thermal dissipation from the CNNs which will be discussed later.

So far, we have analyzed CNN breakdowns in the ON mode. Figure 5a−c show both ON and OFF mode breakdown I_D-V_D curves for CNNs with various percentages of semiconducting SWCNTs. For m-CNNs the breakdown curves are almost linear and identical for both modes (Figure 5a). For s-CNNs, however, in the ON mode the current increases linearly and then saturates before the breakdown (Figures 5c and 3a) while in the OFF mode it remains low at small biases before increasing rapidly at large $|V_D|$ (Figure 5c). Interestingly, J_{max} and V_{BD} values are similar in both ON and OFF modes for CNN devices with similar dimensions and semiconducting tube percentages, rendering the gate voltage ineffective in controlling the breakdown at high bias (see Figure 5d for V_{BD} correlation between ON and OFF modes). This situation occurs because at high fields close to breakdown, semiconducting CNTs turn "ON" due to carrier injection from the contacts and carrier multiplication due to avalanche effects.[37] Avalanche multiplication can occur at relatively low fields (<5 V/μm) in semiconducting SWCNTs,[37] comparable to or lower than the fields observed at thermal breakdown.[38] The observation of both similar J_{max} and similar V_{BD} values in ON and OFF modes also suggests that at high enough lateral fields, properties of barriers between tubes or between tubes and metal electrodes are almost gate independent. These results indicate that removal of metallic CNTs by electrical breakdown *after* fabrication of CNN-TFTs with high tube densities is very challenging due to the ineffective gate control.[28,35] Sorting the semiconducting tubes before the fabrication, hence, is a more viable solution.

Thermal Infrared (IR) Imaging Results. We measured IR thermal radiation from CNN devices at high bias to improve our understanding of the breakdown and heat dissipation mechanisms. Figure 6a shows the imaged temperature of a m-CNN device at high bias close to breakdown. Although hot spots within the CNN and at

the SWCNT junctions reach up to 600 °C at breakdown,[27] the raw temperature captured by the IR camera represents IR radiation generated or reflected from near the top of the Si substrate. (The thin SWCNT film and SiO_2 are effectively transparent to IR.) Nevertheless, the imaged temperature can be converted into an average device temperature as described elsewhere,[27,39] but more immediately the imaged temperature distribution can reveal nonuniformities due to variations in morphology, semiconducting behavior, or nanotube bundling. In the case of m-CNNs imaged here the temperature profile is smooth, indicative of the homogeneity of the m-CNN within the resolution of the IR microscope (~2 μm).

Figure 6 panels b and c show cross sections of the temperature profile in the middle of the m-CNN device along its length (x) and width (y), confirming the smooth temperature decrease from the middle of the CNN. A comparison between the two cross-sectional profiles shows that the temperature drops rather quickly (approaching the background value, here ~70 °C) in the x-direction under the metal contacts (Figure 6b). In contrast, the temperature decrease from the CNN edges in the y-direction (Figure 6c) happens over a considerably longer distance. Estimated heat transfer lengths, L_T (distance over which ΔT drops by a factor of 1/e, see Figure 6b,c), for heat dissipation through the metal contacts are ~8 and ~4 μm for the source and drain electrodes (Figure 6b). Thermal transfer lengths from the edges of the m-CNN to the SiO_2 are ~14 and 15 μm (Figure 6c). The lower L_T values for metal contacts highlight their effectiveness in heat removal from the device, but their asymmetry also suggests asymmetry in the electrical and thermal resistance of the contacts. We observe similar temperature profiles for s-CNNs close to their breakdown (Supporting Information, Figure S10), except that the maximum temperatures are smaller than those for m-CNNs. The smaller temperature rise in s-CNNs correlates well with the lower P_{max} values for these networks as discussed above.

On the basis of the above observations we can estimate average thermal resistances of the m- and s-CNNs near their breakdown. For this purpose, we assume an in-air breakdown temperature[38,40] of 600 °C and subtract the temperature drop across the Si/SiO_2 substrates and across the interface between SWCNTs and oxide[27,38] (see Supporting Information section E). Figure 6d shows that the intrinsic thermal resistance of m-CNNs is on average a factor of 2 lower than those for s-CNNs, at similar network densities and morphologies. Since thermal transport through CNNs is dominated by SWCNT junctions, these results suggest a lower thermal resistance at metallic SWCNT junctions compared to semiconducting SWCNT junctions. These findings are in contrast with recent measurements of SWCNT-surfactant properties in liquid solutions, where the interface thermal resistance was shown to be lower for semiconducting SWCNTs.[41] That observation was

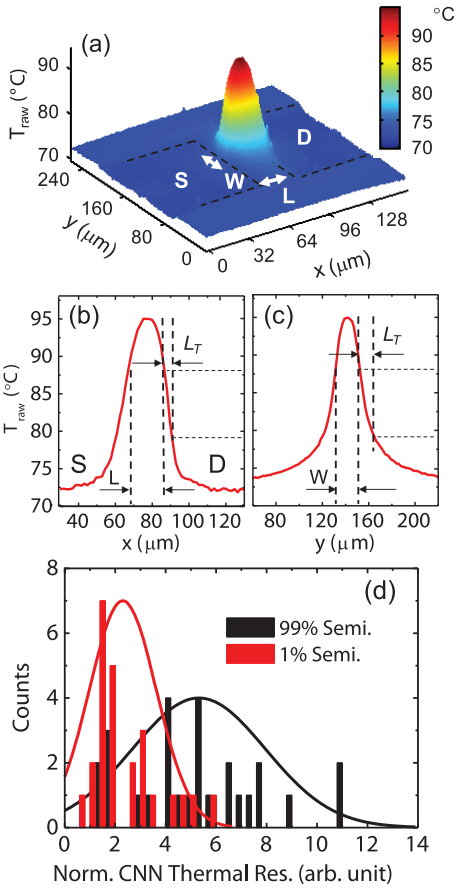

Figure 6. (a) Temperature profile of a metallic CNN with L/W = 15/20 μm close to the breakdown point. V_D = 32 V, V_G = −15 V, P_{max} = 6 mW/μm and t_{ox} = 90 nm. Dashed lines show borders of source (S) and drain (D) contacts. (b and c) Cross-sectional temperature profiles in the middle of the channel along the length (x) and width (y) of the device. Dashed lines in panels b and c show the contacts (L), the edges of the CNN (W), and the thermal transfer lengths (L_T). (d) Distribution of the normalized CNN thermal resistance (removing thermal resistance of the substrate and interface, and normalizing to device area) for purified semiconducting and metallic CNNs.

explained by the higher defect density in semiconducting tubes and the assumption that thermal resistance is mediated by internal phonon coupling. It is possible that the presence of the solid SiO_2 substrate in our case shortens SWCNT phonon lifetimes, as shown by recent molecular dynamics (MD) simulations.[42] (Consistent findings were reported experimentally for SiO_2-supported graphene films, where phonon lifetimes decrease with the layer number.[43]) This, in turn would affect and rebalance the heat dissipation pathways from the CNN. In addition, metallic SWCNTs also benefit from higher electron density, perhaps indicating that electrons play a role in thermal coupling at SWCNT junctions, or between SWCNTs and the SiO_2 substrate.[44] Nevertheless, future work is needed to further resolve such issues, for instance through experiments on individual SWCNTs (by electronic type) and SWCNT junctions[12] rather than on CNNs.

Regardless of their inherent properties, CNNs of all types would be able to tolerate higher levels of current and power densities if better heat dissipation paths through the substrate or contacts were created. For example, using a more thermally conductive (but electrically insulating) substrate material or a substrate with a smoother surface (smaller SWCNT−substrate interface resistance) would assist in dissipating the heat.[45,46] The former is challenging in CNN devices and circuits on flexible substrates which are typically rubbers or plastics, with thermal conductivity even lower (~0.2 W m^{-1} K^{-1}) than the SiO_2 used here (~1.4 W m^{-1} K^{-1}). However, the latter could be achieved, for example, through surface functionalization of SWCNTs for improved thermal coupling.[47,48]

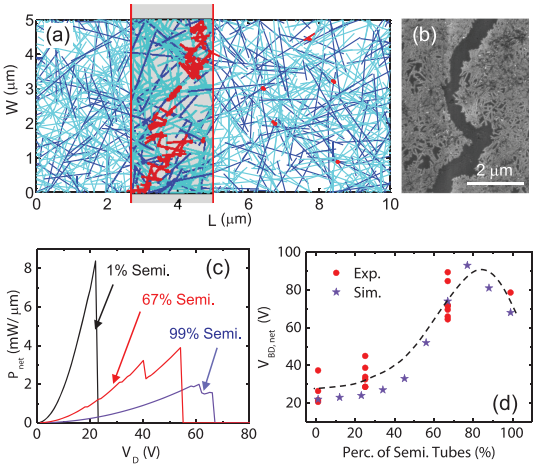

Figure 7. (a) Schematic of the SWCNTs in a simulated 67% semiconducting CNN after electrical breakdown. Semiconducting, metallic, and burned tubes are shown in cyan (light thin), dark blue (dark thin), and red (thick), respectively. The path of burned tubes across the width of the device is clearly noted. The remainder of the CNN parameters are L/W = 10/5 μm and SWCNT density ρ = 12 μm^{-2}. (b) SEM image of the breakdown profile across the width of a 67% semiconducting CNN. (c) Computed net P *vs* V_D for various percentages of semiconducting tubes; $\rho = 12\ \mu m^{-2}$, $L/W = 15/5\ \mu$m. The trends are comparable to Figure 3a and those observed in previous experiments.[27] (d) Experimental and simulated V_{BD} *vs* percentage of semiconducting SWCNTs. L = 15 μm, W = 5 μm. For simulations ρ = 12 μm^{-2}. Dashed line is a guide to the eye.

Computational Analysis. To enhance our understanding of power dissipation in CNNs and to statistically analyze the effect of other parameters on CNN performance, we have developed a Monte Carlo computational platform. SWCNTs are randomly generated in this platform to form a CNN device with desirable parameters.[49] Then, electrical and thermal transport equations are solved self-consistently as a function of applied bias up to the CNN breakdown point (see Methods section and Supporting Information Section E).

Figure 7a illustrates the distribution of SWCNTs in a computer-generated CNN device after breakdown. Broken portions of SWCNTs are highlighted in red. A few isolated hot spots, distributed throughout the device before breakdown, eventually initiate the complete breakdown of the CNN, forming the zigzag gap across the device width (see the Supporting Information movie). The size and shape of the simulated breakdown gaps are very similar to those in our experiments (compare Figure 7a with Figures 3b and 7b, and Supporting Information, Figure S9b). Figure 7c shows net power density *vs* V_D for CNNs with various percentages of semiconducting tubes. V_{BD} and $P_{max,net}$ values are comparable to the experimental results presented in Figure 4 panels a and c, respectively. The agreement between average experimental and simulated V_{BD} values in CNNs with various percentages of semiconducting SWCNTs is shown in Figure 7d (computational values are averages of 200 data points).

The simulations also indicate that differences in density, location, and orientation of SWCNTs within CNN devices (which otherwise have same dimensions) can result in surprisingly substantial variations in device performance. V_{BD} and its distribution vary considerably, for example, with the percentage of semiconducting SWCNTs (Figure 8a) or tube density, ρ (Figure 8b). The homogeneity of the network structure in m-CNNs and the low resistance of metallic SWCNT junctions result in a low average V_{BD} value with relatively narrow distribution. On the other hand, V_{BD} for mixed CNNs is on average higher and can vary over a wide range (Figure 8a). The V_{BD} distribution is also broader for sparse CNNs, where a wider, more random

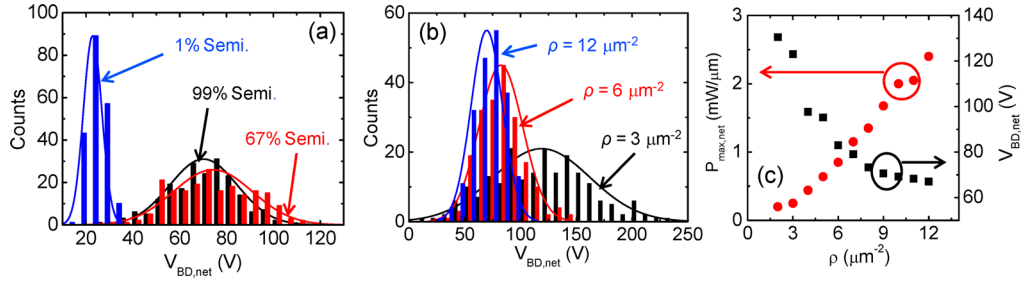

Figure 8. Simulated distribution of $V_{BD,net}$ for (a) various percentages of semiconducting SWCNTs in a CNN with nanotube density ρ = 12 μm^{-2} and (b) various densities of SWCNTs in a 99% semiconducting CNN. (c) Simulated average values of $P_{max,net}$ and $V_{BD,net}$ as a function of ρ for a 99% semiconducting CNN. L = 15 μm and W = 5 μm for all of the CNNs and 200 data points are collected for all of the plots.

range of current paths, network resistance and V_{BD} values can exist (Figure 8b).

An increase in network density ρ also lowers the average values of V_{BD} and raises average values of $P_{max,net}$ (Figure 8c), since it adds new current paths and reduces the overall CNN resistance. As expected, the effect is more dramatic for sparse CNNs. Figure 8c limits density levels up to 12 μm^{-2} because our computational analysis applies to thin, single-layer CNNs. If the density and thickness of the CNNs increase further, nanotubes in top layers will have less access to the substrate which, in turn, would make their heat sinking even less efficient.

CONCLUSIONS

In summary, we have fabricated CNN devices with controlled ratios of metallic and semiconducting SWCNTs (*e.g.*, from <1 to >99% semiconducting proportion), and characterized them electrically, with thermal IR imaging, and detailed computational models. Such results represent (to our knowledge) the first systematic electrical, thermal, and reliability characterization of controlled-purity (sorted) CNN devices. From a fundamental point of view, this work uncovers intrinsic thermal properties of the CNNs suggesting that metallic−metallic nanotube junctions have lower thermal resistance than semiconducting−semiconducting junctions. The lower thermal resistance in metallic junctions could be partially due to the contribution of charge carriers to heat flow across the junctions. From a technological point of view, we find that the high-field performance of such devices differs depending on the semiconducting (*vs* metallic) makeup of the CNNs, and could be improved by carefully engineered heat dissipation. Although individual semiconducting SWCNTs can often carry higher currents due to avalanche carrier multiplication,[37] metallic networks tolerate higher current levels due to the lower junction resistance between metallic SWCNTs. In addition, our study provides important guidelines about the reliability limitations of CNNs for transistor and interconnect applications on flexible substrates, where such aspects will be essential due to the low substrate thermal conductivity.

METHODS

Preparation of SWCNT Dispersions. SWCNT solutions containing different electronic tube types are obtained by density gradient ultracentrifugation (DGU).[19] CNTs synthesized by arc discharge method (P2, Carbon Solutions, Inc.) were used as starting materials for all the samples. The electronic type content was characterized *via* optical absorbance measurements in a Varian Cary 5000 spectrophotometer (Figures S1−S4 in Supporting Information). To quantify semiconducting SWCNT percentage levels, first background absorbance for metallic SWCNTs (blue curves in Figures S1−S4) and next semiconducting SWCNTs (red curves in Figures S1−S4) were subtracted from the absorbance curve, to obtain black curves in Figures S1−S4. Then, semiconducting (metallic) tube percentage was obtained by calculating the area under the S22 (M11 peaks) divided by the total area under S22 and M11 peaks (Figures S1−S4).

The 99% and 67% semiconducting SWCNTs were obtained following a 2-step DGU procedure. The first step was used to extract 25 solutions containing semiconducting percentage levels varying from 98% to 62%. One of the solutions with 67% semiconducting SWCNTs was used directly for device fabrication (Supporting Information, Figure S2). Two of the solutions containing >98% semiconducting SWCNTs were combined for a second DGU iteration to isolate >99% semiconducting SWCNTs.[31] Similarly, metallic SWCNT solutions were obtained from the first step of the DGU for isolating metallic CNTs,[50] after which 26 solutions were obtained with metallic fractions ranging from 99% to 75%. Solutions with 99% metallic (1% semiconducting) SWCNTs and 75% metallic (25% semiconducting SWCNTs) were used directly for device fabrication.

Device Fabrication. Sorted SWCNT solutions were thoroughly dialyzed (Slide-A-Lyzer Dialysis Cassettes, 20 K MWCO, 0.5 mL, Pierce Biotechnology, Inc.) for 2−3 days in ∼6 L of an aqueous 1% weight/volume sodium cholate (SC) solution to remove the density gradient medium iodixanol. Concentration of the dialyzed SWCNTs solutions was adjusted to equalize the sum of the areas under the S22 and M11 absorbance peaks for different semiconducting tube percentage levels. On the basis of previous experiments, two different volumes of SWCNT solutions (45 and 55 μL) were prepared to achieve different densities of CNNs, and these solutions were further diluted with 2 mL of 1% SC:DI H_2O. The diluted solutions were vacuum filtered through mixed cellulose ester membranes (Millipore, pore size = 50 nm, area = 1.42 cm^2) followed by rinsing with ∼100 mL of water to remove the residual surfactant.

CNN devices were fabricated on 300 and 100 nm thermally grown SiO_2 on highly doped Si substrates. First source and drain electrodes (Cr/Au: 1/50 nm) were fabricated by photolithography, thermal evaporation and lift-off processes. CNNs were then transferred from cellulose membranes onto the patterned electrodes under acetone vapors. The substrates were soaked in acetone overnight to remove residual cellulose and were further cleaned by annealing at 230 °C for 1 h in ambient. A second step of photolithography and reactive ion etching (RIE) using O_2 plasma (100 W, 15 s, 200 mTorr) was carried out to define 350 individual CNN devices per chip with lengths $L = 2$ to 150 μm and widths $W = 5$ to 150 μm. The same process was used for fabrication of all the chips with the various percentages of semiconducting SWCNTs and tube densities.

Device Characterization. Fabricated samples were characterized in ambient environment using a Cascade Microtech probe station and Keithley source-meters. IR imaging was performed using a QFI InfraScope II thermal imaging setup with wavelength range of 2−5 μm and best temperature resolution of 0.1 °C. A background temperature of 70 °C was applied to the Si substrate to achieve a high level of sensitivity.[39]

Monte Carlo Simulations. The computational platform for modeling the transport in CNNs was developed by generating SWCNTs with lengths (L_{CNT}) and diameters (d) that are either fixed or randomly determined, based on the distributions obtained from the experiments (see Supporting Information section A).[49] SWCNTs were generated one-by-one within the device area ($L \times W$) until the desired density per unit area (ρ) was obtained. The electronic type of SWCNTs (semiconducting or metallic) was also determined randomly in proportion to the prescribed percentage of the semiconducting SWCNTs in the CNN.

Initial current continuity equations were solved in a matrix format at small V_D by assigning appropriate resistance values to SWCNT segments and their junctions with each other and the metal electrodes (see Supporting Information section E).[51] The model could be improved by adding effects of SWCNT bundling, bending[52], and buckling at the junctions.[53] Once electrical current levels were obtained, the CNN temperature profile was

determined from the thermal transport equations, taking the power dissipation in the CNN nodes as an input. Parameters that were incorporated into the model for thermal calculations were thermal conductivity or conductance values for SiO_2, Si substrates, SWCNT segments, SWCNT−SWCNT junctions, and SWCNT-electrode junctions, in addition to the thermal conductance at the interface between the SWCNTs and SiO_2 (see Supporting Information section E). Broken segments of the CNN (with $T > 600$ °C) were then identified and removed from the network (if any), after which electrical and thermal calculations were repeated to obtain updated power and temperature information. This process was then iterated until no new broken segments could be identified. Next, V_D was increased to its next value, the electrical and thermal parameters were updated, and the recursive electrical and thermal analysis was repeated. V_D was gradually increased until the network became nonconductive, marking the final breakdown point (see Supporting Information, Figure S11).

Conflict of Interest: The authors declare no competing financial interest.

Acknowledgment. The work at University of Illinois Urbana−Champaign (UIUC) was in part supported by the Nanotechnology Research Initiative (NRI), National Science Foundation (NSF, ECCS-0954423) and Army Research Office (W911NF-11-1-0066). The work at Northwestern University (NU) was supported by NSF (DMR-1006391 and DMR-1121262) and the NRI at the NU Materials Research Center. D.E. acknowledges support from the NSF Graduate Research Fellowship program.

Supporting Information Available: Details of the optical absorbance and AFM measurements on SWCNTs in solutions and in fabricated CNN devices; further analysis of CNN characteristics and breakdown properties; additional IR-imaging results for pure s-CNNs; detailed explanation of the parameters used in the computational model. A movie showing a simulation of the CNN breakdown process has also been provided. This material is available free of charge *via* the Internet at http://pubs.acs.org.

REFERENCES AND NOTES

1. Estrada, D.; Dutta, S.; Liao, A.; Pop, E. Reduction of Hysteresis for Carbon Nanotube Mobility Measurements Using Pulsed Characterization. *Nanotechnology* **2010**, *21*, 085702.
2. Pop, E.; Mann, D.; Wang, Q.; Goodson, K.; Dai, H. J. Thermal Conductance of an Individual Single-Wall Carbon Nanotube above Room Temperature. *Nano Lett.* **2006**, *6*, 96–100.
3. Sangwan, V. K.; Behnam, A.; Ballarotto, V. W.; Fuhrer, M. S.; Ural, A.; Williams, E. D. Optimizing Transistor Performance of Percolating Carbon Nanotube Networks. *Appl. Phys. Lett.* **2010**, *97*, 043111.
4. Hone, J.; Whitney, M.; Piskoti, C.; Zettl, A. Thermal Conductivity of Single-Walled Carbon Nanotubes. *Phys. Rev. B* **1999**, *59*, R2514–R2516.
5. Snow, E. S.; Novak, J. P.; Campbell, P. M.; Park, D. Random Networks of Carbon Nanotubes as an Electronic Material. *Appl. Phys. Lett.* **2003**, *82*, 2145–2147.
6. Itkis, M. E.; Borondics, F.; Yu, A. P.; Haddon, R. C. Thermal Conductivity Measurements of Semitransparent Single-Walled Carbon Nanotube Films by a Bolometric Technique. *Nano Lett.* **2007**, *7*, 900–904.
7. Kim, D. H.; Huang, J.; Shin, H. K.; Roy, S.; Choi, W. Transport Phenomena and Conduction Mechanism of Single-walled Carbon Nanotubes (SWNTs) at Y- and Crossed-junctions. *Nano Lett.* **2006**, *6*, 2821–2825.
8. Tombler, T. W.; Zhou, C. W.; Kong, J.; Dai, H. J. Gating Individual Nanotubes and Crosses with Scanning Probes. *Appl. Phys. Lett.* **2000**, *76*, 2412–2414.
9. Nirmalraj, P. N.; Lyons, P. E.; De, S.; Coleman, J. N.; Boland, J. J. Electrical Connectivity in Single-Walled Carbon Nanotube Networks. *Nano Lett.* **2009**, *9*, 3890–3895.
10. Fuhrer, M. S.; Nygard, J.; Shih, L.; Forero, M.; Yoon, Y. G.; Mazzoni, M. S. C.; Choi, H. J.; Ihm, J.; Louie, S. G.; Zettl, A.; McEuen, P. L. Crossed Nanotube Junctions. *Science* **2000**, *288*, 494–497.
11. Lee, E. J. H.; Balasubramanian, K.; Burghard, M.; Kern, K. Spatially Resolved Potential Distribution in Carbon Nanotube Cross-Junction Devices. *Adv. Mater.* **2009**, *21*, 2720–2724.
12. Yang, J. K.; Waltermire, S.; Chen, Y. F.; Zinn, A. A.; Xu, T. T.; Li, D. Y. Contact Thermal Resistance between Individual Multiwall Carbon Nanotubes. *Appl. Phys. Lett.* **2010**, *96*, 023109.
13. Zhong, H. L.; Lukes, J. R. Interfacial Thermal Resistance between Carbon Nanotubes: Molecular Dynamics Simulations and Analytical Thermal Modeling. *Phys. Rev. B* **2006**, *74*, 125403.
14. Prasher, R. S.; Hu, X. J.; Chalopin, Y.; Mingo, N.; Lofgreen, K.; Volz, S.; Cleri, F.; Keblinski, P. Turning Carbon Nanotubes from Exceptional Heat Conductors into Insulators. *Phys. Rev. Lett.* **2009**, *102*, 105901.
15. Volkov, A. N.; Zhigilei, L. V. Scaling Laws and Mesoscopic Modeling of Thermal Conductivity in Carbon Nanotube Materials. *Phys. Rev. Lett.* **2010**, *104*, 215902.
16. Evans, W. J.; Shen, M.; Keblinski, P. Inter-tube Thermal Conductance in Carbon Nanotubes Arrays and Bundles: Effects of Contact Area and Pressure. *Appl. Phys. Lett.* **2012**, *100*, 261908.
17. Jariwala, D.; Sangwan, V. K.; Lauhon, L. J.; Marks, T. J.; Hersam, M. C. Carbon Nanomaterials for Electronics, Optoelectronics, Photovoltaics, and Sensing. *Chem. Soc. Rev.* **2013**, 10.1039/c2cs35335k.
18. Wang, C.; Zhang, J. L.; Ryu, K. M.; Badmaev, A.; De Arco, L. G.; Zhou, C. W. Wafer-Scale Fabrication of Separated Carbon Nanotube Thin-Film Transistors for Display Applications. *Nano Lett.* **2009**, *9*, 4285–4291.
19. Arnold, M. S.; Green, A. A.; Hulvat, J. F.; Stupp, S. I.; Hersam, M. C. Sorting Carbon Nanotubes by Electronic Structure Using Density Differentiation. *Nat. Nanotechnol.* **2006**, *1*, 60–65.
20. Engel, M.; Small, J. P.; Steiner, M.; Freitag, M.; Green, A. A.; Hersam, M. C.; Avouris, P. Thin Film Nanotube Transistors Based on Self-Assembled, Aligned, Semiconducting Carbon Nanotube Arrays. *ACS Nano* **2008**, *2*, 2445–2452.
21. Timmermans, M. Y.; Estrada, D.; Nasibulin, A. G.; Wood, J. D.; Behnam, A.; Sun, D. M.; Ohno, Y.; Lyding, J. W.; Hassanien, A.; Pop, E.; Kauppinen, E. I. Effect of Carbon Nanotube Network Morphology on Thin Film Transistor Performance. *Nano Res.* **2012**, *5*, 307–319.
22. Choi, S.-J.; Wang, C.; Lo, C. C.; Bennett, P.; Javey, A.; Bokor, J. Comparative Study of Solution-Processed Carbon Nanotube Network Transistors. *Appl. Phys. Lett.* **2012**, *101*, 112104–4.
23. Sun, D. M.; Timmermans, M. Y.; Tian, Y.; Nasibulin, A. G.; Kauppinen, E. I.; Kishimoto, S.; Mizutani, T.; Ohno, Y. Flexible High-Performance Carbon Nanotube Integrated Circuits. *Nat. Nanotechnol.* **2011**, *6*, 156–161.
24. Cao, Q.; Kim, H. S.; Pimparkar, N.; Kulkarni, J. P.; Wang, C. J.; Shim, M.; Roy, K.; Alam, M. A.; Rogers, J. A. Medium-Scale Carbon Nanotube Thin-Film Integrated Circuits on Flexible Plastic Substrates. *Nature* **2008**, *454*, 495–500.
25. Kim, S.; Kim, S.; Park, J.; Ju, S.; Mohammadi, S. Fully Transparent Pixel Circuits Driven by Random Network Carbon Nanotube Transistor Circuitry. *ACS Nano* **2010**, *4*, 2994–2998.
26. Topinka, M. A.; Rowell, M. W.; Goldhaber-Gordon, D.; McGehee, M. D.; Hecht, D. S.; Gruner, G. Charge Transport in Interpenetrating Networks of Semiconducting and Metallic Carbon Nanotubes. *Nano Lett.* **2009**, *9*, 1866–1871.
27. Estrada, D.; Pop, E. Imaging Dissipation and Hot Spots in Carbon Nanotube Network Transistors. *Appl. Phys. Lett.* **2011**, *98*, 073102.
28. Shekhar, S.; Erementchouk, M.; Leuenberger, M. N.; Khondaker, S. I. Correlated Electrical Breakdown in Arrays of High Density Aligned Carbon Nanotubes. *Appl. Phys. Lett.* **2011**, *98*, 243121.
29. Strus, M. C.; Chiaramonti, A. N.; Kim, Y. L.; Jung, Y. J.; Keller, R. R. Accelerated Reliability Testing of Highly Aligned Single-Walled Carbon Nanotube Networks Subjected to DC Electrical Stressing. *Nanotechnology* **2011**, *22*, 265713.
30. Behnam, A.; Noriega, L.; Choi, Y.; Wu, Z. C.; Rinzler, A. G.; Ural, A. Resistivity Scaling in Single-Walled Carbon

Nanotube Films Patterned to Submicron Dimensions. *Appl. Phys. Lett.* **2006**, *89*, 093107.
31. Sangwan, V. K.; Ponce Ortiz, R.; Alaboson, J. M. P.; Emery, J. D.; Bedzyk, M. J.; Lauhon, L. J.; Marks, T. J.; Hersam, M. C. Fundamental Performance Limits of Carbon Nanotube Thin-Film Transistors Achieved Using Hybrid Molecular Dielectrics. *ACS Nano* **2012**, *6*, 7480–7488.
32. Rouhi, N.; Jain, D.; Burke, P. J. High-Performance Semiconducting Nanotube Inks: Progress and Prospects. *ACS Nano* **2011**, *5*, 8471–8487.
33. Schroder, D. K., *Semiconductor Material and Device Characterization*, 3rd ed.; John Wiley & Sons: Hoboken, 2006; p 139.
34. Kang, S. J.; Kocabas, C.; Ozel, T.; Shim, M.; Pimparkar, N.; Alam, M. A.; Rotkin, S. V.; Rogers, J. A. High-Performance Electronics Using Dense, Perfectly Aligned Arrays of Single-Walled Carbon Nanotubes. *Nat. Nanotechnol.* **2007**, *2*, 230–236.
35. Wang, C. A.; Ryu, K. M.; De Arco, L. G.; Badmaev, A.; Zhang, J. L.; Lin, X.; Che, Y. C.; Zhou, C. W. Synthesis and Device Applications of High-Density Aligned Carbon Nanotubes Using Low-Pressure Chemical Vapor Deposition and Stacked Multiple Transfer. *Nano Res.* **2010**, *3*, 831–842.
36. Yanagi, K.; Udoguchi, H.; Sagitani, S.; Oshima, Y.; Takenobu, T.; Kataura, H.; Ishida, T.; Matsuda, K.; Maniwa, Y. Transport Mechanisms in Metallic and Semiconducting Single-Wall Carbon Nanotube Networks. *ACS Nano* **2010**, *4*, 4027–4032.
37. Liao, A.; Zhao, Y.; Pop, E. Avalanche-Induced Current Enhancement in Semiconducting Carbon Nanotubes. *Phys. Rev. Lett.* **2008**, *101*, 256804.
38. Liao, A.; Alizadegan, R.; Ong, Z. Y.; Dutta, S.; Xiong, F.; Hsia, K. J.; Pop, E. Thermal Dissipation and Variability in Electrical Breakdown of Carbon Nanotube Devices. *Phys. Rev. B* **2010**, *82*, 205406.
39. Bae, M. H.; Ong, Z. Y.; Estrada, D.; Pop, E. Imaging, Simulation, and Electrostatic Control of Power Dissipation in Graphene Devices. *Nano Lett.* **2010**, *10*, 4787–4793.
40. Hata, K.; Futaba, D. N.; Mizuno, K.; Namai, T.; Yumura, M.; Iijima, S. Water-Assisted Highly Efficient Synthesis of Impurity-free Single-Walled Carbon Nanotubes. *Science* **2004**, *306*, 1362–1364.
41. Kang, S. D.; Lim, S. C.; Lee, E. S.; Cho, Y. W.; Kim, Y. H.; Lyeo, H. K.; Lee, Y. H. Interfacial Thermal Conductance Observed to be Higher in Semiconducting than Metallic Carbon Nanotubes. *ACS Nano* **2012**, *6*, 3853–3860.
42. Ong, Z.-Y.; Pop, E.; Shiomi, J. Reduction of Phonon Lifetimes and Thermal Conductivity of a Carbon Nanotube on Amorphous Silica. *Phys. Rev. B* **2011**, *84*, 165418.
43. Kang, K.; Abdula, D.; Cahill, D. G.; Shim, M. Lifetimes of Optical Phonons in Graphene and Graphite by Time-Resolved Incoherent Anti-Stokes Raman Scattering. *Phys. Rev. B* **2010**, *81*, 165405.
44. Rotkin, S. V.; Perebeinos, V.; Petrov, A. G.; Avouris, P. An Essential Mechanism of Heat Dissipation in Carbon Nanotube Electronics. *Nano Lett.* **2009**, *9*, 1850–1855.
45. Liao, A. D.; Wu, J. Z.; Wang, X. R.; Tahy, K.; Jena, D.; Dai, H. J.; Pop, E. Thermally Limited Current Carrying Ability of Graphene Nanoribbons. *Phys. Rev. Lett.* **2011**, *106*, 256801.
46. Behnam, A.; Lyons, A. S.; Bae, M.-H.; Chow, E. K.; Islam, S.; Neumann, C. M.; Pop, E. Transport in Nanoribbon Interconnects Obtained from Graphene Grown by Chemical Vapor Deposition. *Nano Lett.* **2012**, *12*, 4424–4430.
47. Xu, Z.; Buehler, M. J. Nanoengineering Heat Transfer Performance at Carbon Nanotube Interfaces. *ACS Nano* **2009**, *3*, 2767–2775.
48. Clancy, T. C.; Gates, T. S. Modeling of Interfacial Modification Effects on Thermal Conductivity of Carbon Nanotube Composites. *Polymer* **2006**, *47*, 5990–5996.
49. Hicks, J.; Behnam, A.; Ural, A. Resistivity in Percolation Networks of One-Dimensional Elements with a Length Distribution. *Phys. Rev. E* **2009**, *79*, 012102.
50. Green, A. A.; Hersam, M. C. Colored Semitransparent Conductive Coatings Consisting of Monodisperse Metallic Single-Walled Carbon Nanotubes. *Nano Lett.* **2008**, *8*, 1417–1422.
51. Behnam, A.; Bosman, G.; Ural, A. Percolation Scaling of 1/*f* Noise in Single-Walled Carbon Nanotube Films. *Phys. Rev. B* **2008**, *78*, 085431.
52. Volkov, A. N.; Shiga, T.; Nicholson, D.; Shiomi, J.; Zhigilei, L. V. Effect of Bending Buckling of Carbon Nanotubes on Thermal Conductivity of Carbon Nanotube Materials. *J. Appl. Phys.* **2012**, *111*, 053501.
53. Gupta, M. P.; Chen, L.; Estrada, D.; Behnam, A.; Pop, E.; Kumar, S. Impact of Thermal Boundary Conductances on Power Dissipation and Electrical Breakdown of Carbon Nanotube Network Transistors. *J. Appl. Phys.* **2012**, *112*, 124506.

Supplementary Information

High-Field Transport and Thermal Reliability of Sorted Carbon Nanotube Network Devices

Ashkan Behnam[1,2], Vinod K. Sangwan[3], Xuanyu Zhong[2], Feifei Lian[1,2], David Estrada[1,2], Deep Jariwala[3], Alicia J. Hoag[2], Lincoln J. Lauhon[3], Tobin J. Marks[3,4], Mark C. Hersam[3,4], Eric Pop[1,2,5*]*

[1]Micro and Nanotechnology Lab., Univ. Illinois at Urbana-Champaign, IL 61801, USA

[2]Dept. Electrical & Computer Eng., Univ. Illinois at Urbana-Champaign, IL 61801, USA

[3]Dept. Materials Science & Eng., Northwestern Univ., Evanston, IL 60208, USA

[4]Dept. of Chemistry, Northwestern Univ., Evanston, IL 60208, USA

[5]Beckman Institute, Univ. of Illinois at Urbana-Champaign, Urbana, IL 61801, USA

[*]Contact e-mail: abehnam@illinois.edu and epop@illinois.edu

Section A. Characterization of single-walled carbon nanotube (SWCNT) dispersions and networks (CNNs)

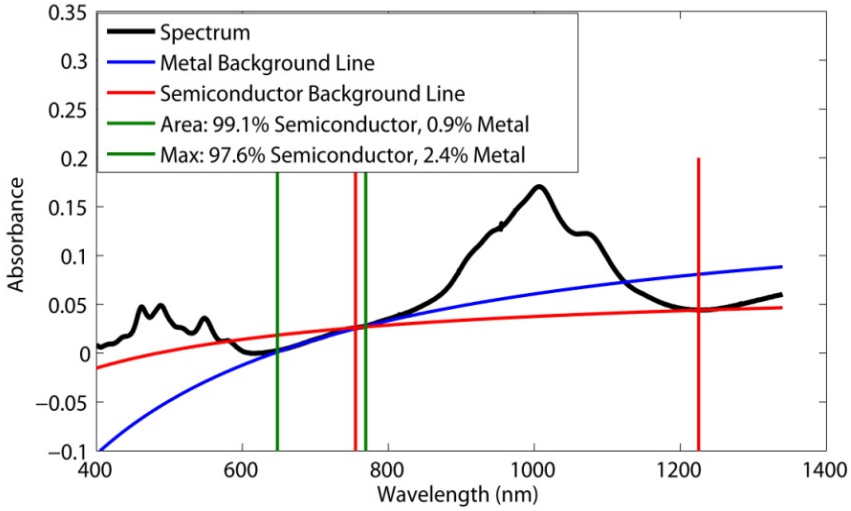

Figure S1. Background subtracted optical absorbance for a 99.1% semiconducting SWCNTs dispersion. The part of black curve between two vertical red lines represents S22 peaks of semiconducting SWCNTs and the part between two vertical green lines represents M11 peaks of metallic SWCNTs.

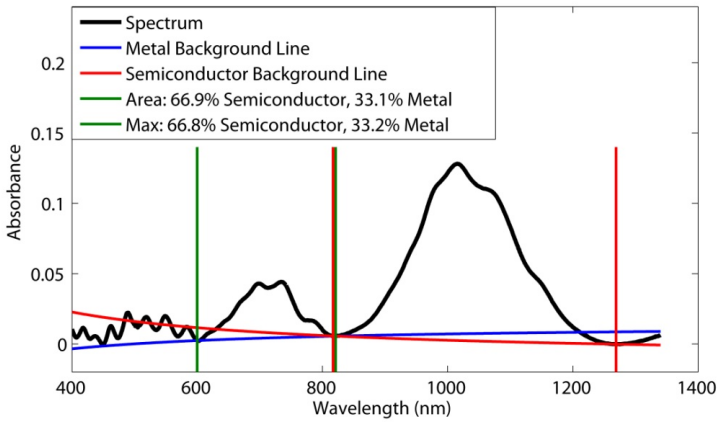

Figure S2. Background subtracted optical absorbance for a 66.9% semiconducting SWCNTs dispersion.

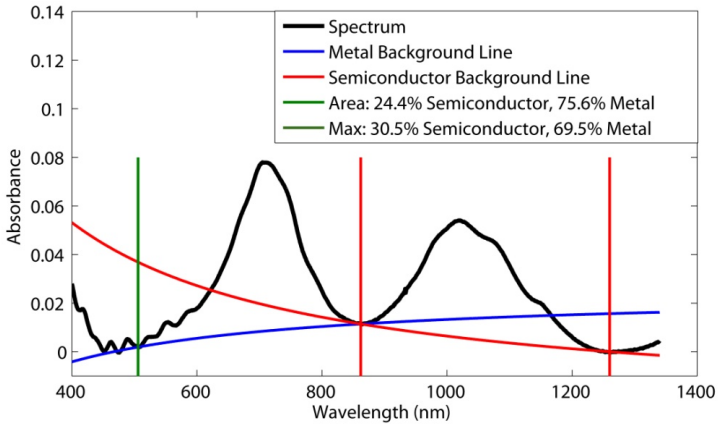

Figure S3. Background subtracted optical absorbance for a 24.4% semiconducting SWCNTs dispersion.

Figure S5a shows as-obtained optical absorbance data for semiconducting purity levels of 99%, 67%, 25% and 1%. Optical absorbance for the solution prepared with 67% semiconducting purity level is similar to that obtained for the as-purchased unsorted carbon nanotubes (Figure S5b).

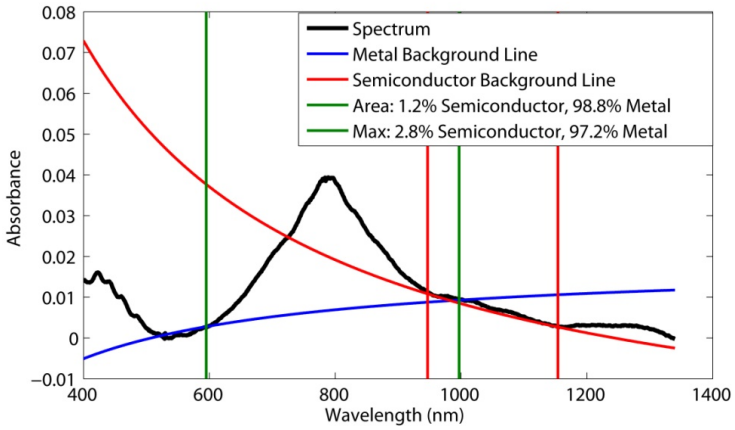

Figure S4. Background subtracted optical absorbance for a 1.2% semiconducting SWCNTs dispersion.

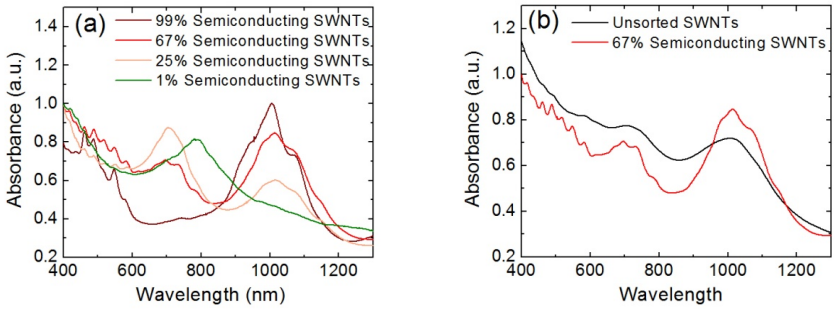

Figure S5. (a) Raw optical absorbance spectra of all dispersions with various semiconducting purity levels. The vertical scale is normalized to the highest peak in each curve. **(b)** Optical absorbance of unsorted (as-purchased arc-discharged) SWCNTs is compared with sorted SWNTs with 67% semiconducting purity.

We have also characterized the diameter of individual SWCNTs by atomic force microscopy (AFM). We drop-casted sparse SWCNT solutions on a Si substrate coated with (3-aminopropyl) triethoxysilane (APTES, Sigma-Aldrich). Figure S6a shows a histogram of the diameter of about 30 SWCNTs. Average diameter of 1.41 nm corresponds well with the diameter range (1.4 nm - 1.5 nm) extracted from the S22 peak in Figure S1. The length distribution of individual SWCNTs obtained by the same AFM procedure is reported elsewhere (average length of 1.36 μm for 330 SWCNTs).[S1]

For comparison, we have also performed Raman spectroscopy on our sorted CNNs (at a wavelength of 632 nm) after device fabrication, as shown in Figure S6b-c. The two radial breathing mode (RBM) peaks observed correspond to SWCNT diameters of 1.4-1.45 nm and 1.55-1.6 nm[S2-S3], which are also consistent with AFM and optical spectra measurements (Figure S6a). On

the G-band, the location and intensity of the G^+ peak at 1591 cm^{-1} appears constant. The relative intensity of the G^- peak at 1567 cm^{-1}, however depends on the percentage of semiconducting SWCNTs in the CNN. Assuming that this G^- peak is due to the contribution of semiconducting tubes, its location corresponds to tubes with average diameter of 1.6 nm. Unfortunately, due to the lack of information about the chirality mixture of SWCNTs in CNNs, analysis of the RBM and G peaks for determining the percentage of SWCNTs at a single incident wavelength is not straightforward[S3]. We therefore, rely on our analysis of the optical spectra described above for determining the percentage of semiconducting tubes in CNNs.

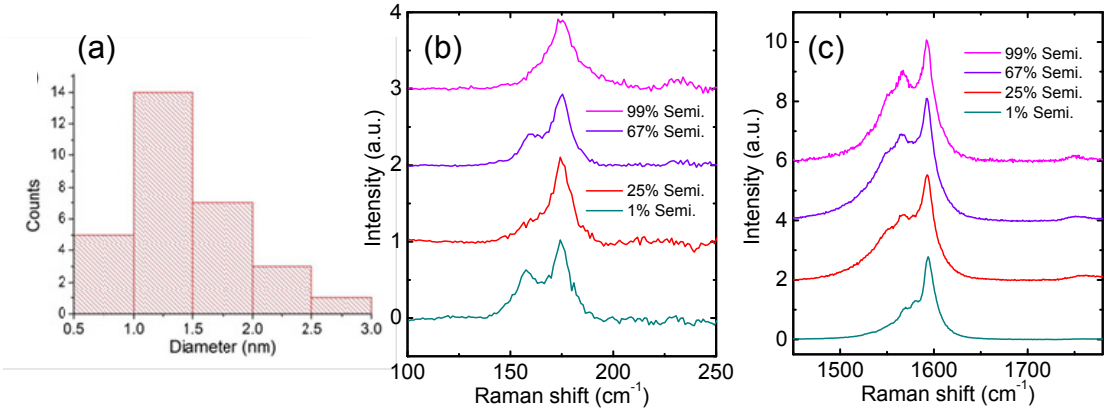

Figure S6. (a) Histogram of the diameter distribution of 30 SWCNTs in a sparse CNN characterized by AFM, showing an average diameter of 1.41 nm. **(b)** RBM and **(c)** G-band Raman spectra of CNN devices with different percentage of semiconducting SWCNTs, suggesting diameters of 1.4-1.45 nm and 1.55-1.6 nm.

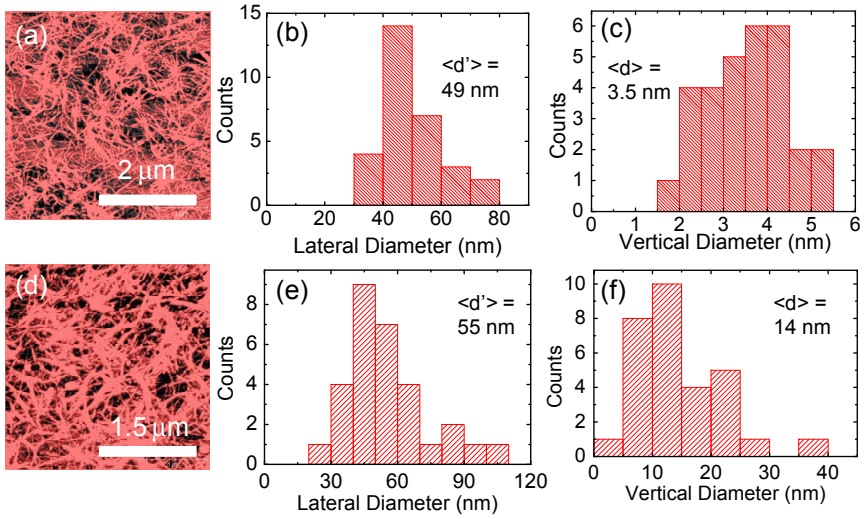

Figure S7. Analysis of network parameters in CNN-TFTs fabricated from CNNs with two different densities. **(a)&(d)** Processed AFM images. Highlighted areas are covered by the network. **(b)&(e)** Tubes apparent lateral diameter *d'* and **(c)&(f)** vertical diameter, *d*, distributions. These diameters are correlated with each other, strongly suggesting individual SWCNTs form varying diameter bundles which then form the CNN.

In addition to studying individual tube properties, we have used AFM to characterize the morphology of the networks in fabricated thin film transistors (CNN-TFTs). As shown in Figures S7c and f, measured vertical diameters are larger than the average diameters of individual tubes suggesting the presence of bundles in these networks. The bundle size seems to increase with the density of the tubes in CNNs as is the case for Figure S7f compared to Figure S7c. Measured lateral widths (diameter) of tube bundles are significantly larger than measured vertical diameters due to the large size of AFM tip and other inaccuracies in measuring lateral dimensions by AFM (Figures S7b and e). Nevertheless, lateral width information is useful for estimating CNN bundle density after fabrication. Percentage of device area covered by nanotube bundles (obtained by processing AFM images) together with the bundle width and length distribution information provide an estimate for bundle density.

Section B. TFT-CNNs device characteristics

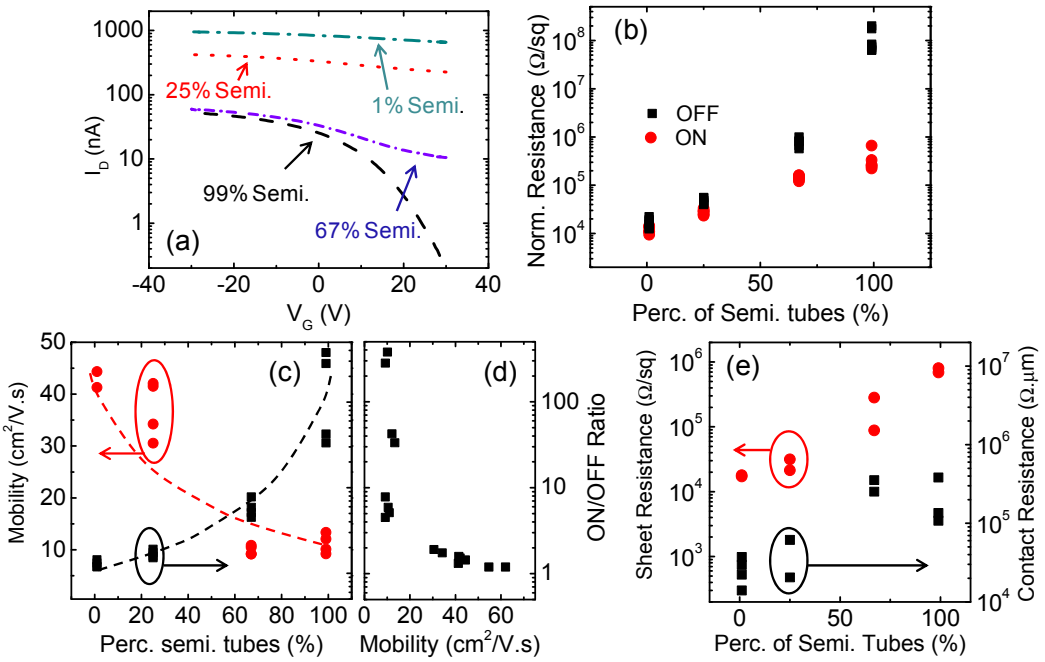

Figure S8. (a) I_D-V_G characteristics for CNNs with various percentage of semiconducting SWCNTs. L = 40 μm, W = 50 μm and V_D = 10 mV. **(b)** & **(c)** & **(d)** Device characteristics for wider structures: **(b)** ON and OFF resistance (normalized to W and L) vs. percentage of semiconducting SWCNTs **(c)** Mobility and ON/OFF ratio vs. percentage of semiconducting SWCNTs within the CNNs. L = 40 or 50 μm and W = 100 μm. **(d)** ON/OFF ratio vs. mobility for the same CNNs. **(e)** Sheet and contact resistances vs. percentage of semiconducting SWCNTs for CNNs with various L and W and at V_G = -30 V. t_{ox} = 300 nm for all the measured devices.

Section C. CNN-TFTs at breakdown

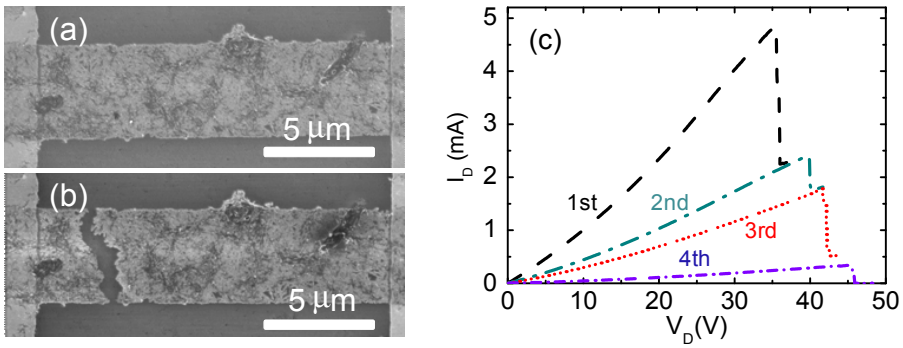

Figure S9. (a) & (b) SEM images of a CNN with L = 15 µm, W = 5 µm and t_{ox} = 300 nm before and after the breakdown. **(c)** I_D-V_D sweeps for partial breakdown of a CNN. V_G = -30 V, L = 15 µm, W = 50 µm and t_{ox} = 300 nm. Voltage sweeps are stopped and repeated after each significant drop in current.

Section D. Temperature profile of CNNs with various percentages of semiconducting SWCNTs

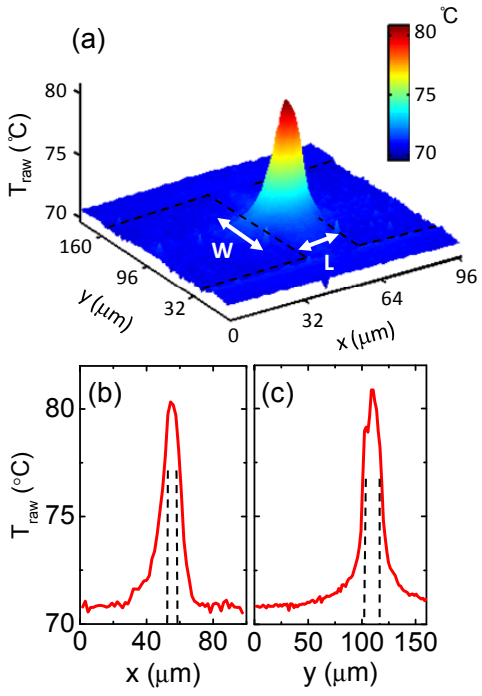

Figure S10. (a) Temperature profile in a 99% semiconducting CNN with L = 5 µm and W = 20 µm close to the breakdown point. V_D = 65 V, V_G = -15 V, P_{max} = 1.25 mW/µm and t_{ox} = 90 nm. Dashed lines show borders of the contacts. **(b) & (c)** Cross-sectional temperature profiles in the middle of the channel along the width (y) and length (x) of the device. Dashed lines in (b) and (c) correspond to the edges of the CNN (W) and the contacts (L), respectively.

Section E. Details of the computational model parameters

We calculate electrical resistance of an individual SWCNT segment using $R_l = R_0 l / \lambda$, where l is the segment length, λ is the temperature dependent mean free path,[S4] and $R_0 = h/4e^2$ is the theoretical contact resistance at the ballistic limit (~ 6.5 kΩ).[S5] The resistance of tube-tube junctions depends on whether the junction is metallic/semiconducting (MS), semiconducting/semiconducting (SS), or metallic/metallic (MM). It has been shown that MS junctions have significantly larger contact resistance than MM junctions due to their Schottky nature. Based on previous experimental studies[S6-S10] and our electrical measurements on purified networks, we use $R_{MM} = 80R_0$, $R_{SS} = 1000R_0$, and $R_{MS} = 800R_0$, where R_{MM}, R_{SS}, and R_{MS} are the contact resistances for MM, SS, and MS junctions, respectively. In addition, we consider a tunneling barrier due to the depletion region created in semiconducting tubes that are in contact with metallic tubes. We incorporate all of these values in the current continuity equations throughout the network which are then solved in the matrix format.[S11]

We take a similar approach for calculating the heat transport through the generated CNNs. However, SiO_2 and Si substrates are thermally conductive (in spite of being electrically isolating) and play a significant role in heat dissipation. Thermal resistivity of SWCNT segments along their length is $\rho_{l,th} = [1983 + 1033\,(1 + 0.5/l)] \times 10^{-7}$ mKW^{-1} (Ref. S12, l in μm) and therefore thermal resistance becomes $R_{l,th} = \lfloor \rho_{l,th}\, l / \pi d b \rfloor \tanh(l_h / l)$ where d is the SWCNT diameter, b ~ 0.35 nm is the thickness of the edge of the tube and l_h is the thermal healing length defined as $l_h = \sqrt{\pi d b / \rho_{l,th} g_{total}}$. The thermal healing length is indicative of the substrate's ability to dissipate heat. g_{total} is the inverse of total substrate thermal resistance per unit length. Substrate thermal resistance consists of:

i) The interface thermal resistance between the SWCNT and the supporting SiO_2, $R_c = 1/(g_c l)$, where g_c is the interface thermal conductance per unit length found to be proportional to the diameter of the SWCNT[S13] ($g_c \sim 0.15d$ $Wm^{-1}K^{-1}$ with d in nm) and almost independent of SWCNT type[S14].

ii) The thermal resistance through the oxide $R_{ox} = 1/(g_{ox} l)$ where $g_{ox} = \pi . k_{ox} / \ln(8 t_{ox} / \pi d)$ with t_{ox} being the oxide thickness and k_{ox} being the thermal conductivity of the oxide (~ 1.3

$Wm^{-1}K^{-1}$).[S15] This equation includes the effect of fringing heat loss from the narrow nanotubes.

iii) The thermal resistance through the Si substrate $R_{Si} = 1/2\, k_{Si} A_{eff}^{1/2}$ where k_{Si} is the thermal conductivity of the Si (~ 100 $Wm^{-1}K^{-1}$) and A_{eff} is the effective area underneath the oxide for heat dissipation.

In addition to the role of the substrate in heat dissipation, thermal resistances at the junctions between SWCNTs or between a SWCNT and metal electrodes should be considered. Since experimental studies have not suggested any significant dependence of the junction resistance on electronic type of the tubes, we use an average resistance (per unit contact area) of $R_{Jnn,th} = 10^{-8}$ $KW^{-1}m^2$ for all types of SWCNT-SWCNT junctions[S16-S20] and average resistance of $R_{Jnm,th} = 10^{7}$ KW^{-1} at the junctions between SWCNTs and metal electrodes.[S21] Based on the above values, tube-tube junction resistance is significantly higher than other resistances in the CNN. It is also proportional to the junction area which varies significantly in the simulated CNNs depending on the angles that nanotubes take with respect to each other (Figure S12a). We incorporate all the thermal resistance values into the model assuming a boundary condition temperature of 300 K at the bottom of Si substrate and at metal electrodes and taking the dissipated power from the current transport through the network as the input.

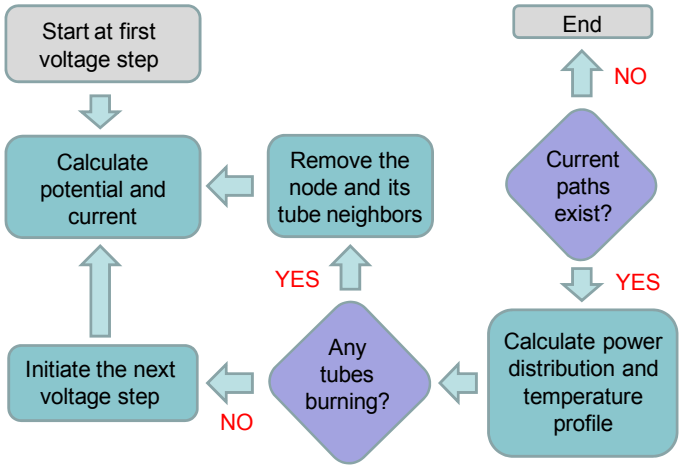

Figure S11. Flow chart showing the steps in simulating the breakdown process in CNNs.

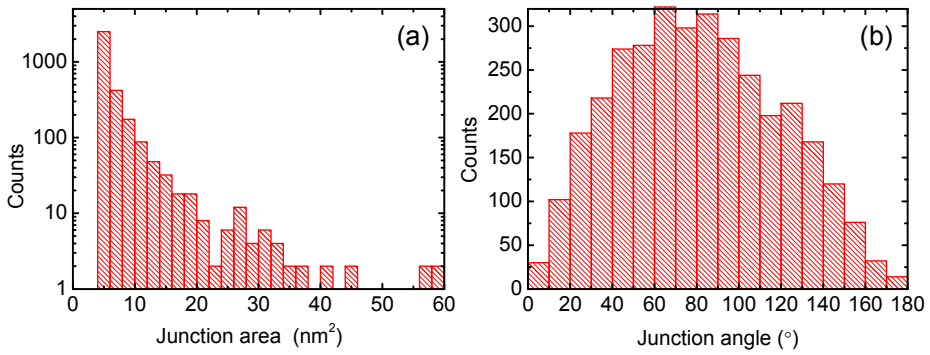

Figure S12. Distribution of **(a)** junction area and **(b)** junction angle for a CNN simulated with fixed nanotube diameter of 2 nm. Junction area significantly increases as junction angle deviates from 90 degrees.

Supplementary References

(S1) Sangwan, V. K.; Ponce Ortiz, R.; Alaboson, J. M. P.; Emery, J. D.; Bedzyk, M. J.; Lauhon, L. J.; Marks, T. J.; Hersam, M. C. Fundamental Performance Limits of Carbon Nanotube Thin-Film Transistors Achieved Using Hybrid Molecular Dielectrics. *ACS Nano* **2012,** *6*, 7480-7488.

(S2) Zheng, M.; Jagota, A.; Strano, M. S.; Santos, A. P.; Barone, P.; Chou, S. G.; Diner, B. A.; Dresselhaus, M. S.; McLean, R. S.; Onoa, G. B.; Samsonidze, G. G.; Semke, E. D.; Usrey, M.; Walls, D. J. Structure-based carbon nanotube sorting by sequence-dependent DNA assembly. *Science* **2003,** *302*, 1545-1548.

(S3) Jorio, A.; Souza, A. G.; Dresselhaus, G.; Dresselhaus, M. S.; Swan, A. K.; Unlu, M. S.; Goldberg, B. B.; Pimenta, M. A.; Hafner, J. H.; Lieber, C. M.; Saito, R. G-band resonant Raman study of 62 isolated single-wall carbon nanotubes. *Phys. Rev. B* **2002,** *65*, 155412.

(S4) Pop, E.; Mann, D.; Reifenberg, J.; Goodson, K.; Dai, H. Electro-thermal Transport in Metallic Single-Wall Carbon Nanotubes for Interconnect Applications *In IEEE Intl. Electron Dev. Meet. (Washington, DC.)* **2005,** 253-256.

(S5) Li, S.; Yu, Z.; Rutherglen, C.; Burke, P. J. Electrical Properties of 0.4 cm Long Single-walled Carbon Nanotubes. *Nano Lett.* **2004**, *4*, 2003-2007.

(S6) Fuhrer, M. S.; Nygard, J.; Shih, L.; Forero, M.; Yoon, Y. G.; Mazzoni, M. S. C.; Choi, H. J.; Ihm, J.; Louie, S. G.; Zettl, A.; McEuen, P. L. Crossed Nanotube Junctions. *Science* **2000,** *288*, 494-497.

(S7) Lee, E. J. H.; Balasubramanian, K.; Burghard, M.; Kern, K. Spatially Resolved Potential Distribution in Carbon Nanotube Cross-Junction Devices. *Adv. Mater.* **2009,** *21*, 2720-2724.

(S8) Nirmalraj, P. N.; Lyons, P. E.; De, S.; Coleman, J. N.; Boland, J. J. Electrical Connectivity in Single-Walled Carbon Nanotube Networks. *Nano Lett.* **2009,** *9*, 3890-3895.

(S9) Kim, D. H.; Huang, J.; Shin, H. K.; Roy, S.; Choi, W. Transport Phenomena and Conduction Mechanism of Single-walled Carbon Nanotubes (SWNTs) at Y- and Crossed-junctions. *Nano Lett.* **2006,** *6*, 2821-2825.

(S10) Tombler, T. W.; Zhou, C. W.; Kong, J.; Dai, H. J. Gating Individual Nanotubes and Crosses with Scanning Probes. *Appl. Phys. Lett.* **2000,** *76*, 2412-2414.

(S11) Behnam, A.; Guo, J.; Ural, A. Effects of Nanotube Alignment and Measurement Direction on Percolation Resistivity in Single-walled Carbon Nanotube Films. *J. Appl. Phys.* **2007,** *102*, 044313.

(S12) Pop, E.; Mann, D.; Wang, Q.; Goodson, K.; Dai, H. J. Thermal Conductance of an Individual Single-wall Carbon Nanotube above Room Temperature. *Nano Lett.* **2006,** *6*, 96-100.

(S13) Ong, Z. Y.; Pop, E. Molecular Dynamics Simulation of Thermal Boundary Conductance Between Carbon Nanotubes and SiO2. *Phys. Rev. B* **2010,** *81*, 155408.

(S14) Liao, A.; Alizadegan, R.; Ong, Z. Y.; Dutta, S.; Xiong, F.; Hsia, K. J.; Pop, E. Thermal Dissipation and Variability in Electrical Breakdown of Carbon Nanotube Devices. *Phys. Rev. B* **2010,** *82*, 205406.

(S15) Pop, E.; Mann, D. A.; Goodson, K. E.; Dai, H. J. Electrical and Thermal Transport in Metallic Single-wall Carbon Nanotubes on Insulating Substrates. *J. Appl. Phys.* **2007,** *101*, 093710.

(S16) Estrada, D.; Pop, E. Imaging Dissipation and Hot Spots in Carbon Nanotube Network Transistors. *Appl. Phys. Lett.* **2011,** *98*, 073102.

(S17) Prasher, R. S.; Hu, X. J.; Chalopin, Y.; Mingo, N.; Lofgreen, K.; Volz, S.; Cleri, F.; Keblinski, P. Turning Carbon Nanotubes from Exceptional Heat Conductors into Insulators. *Phys. Rev. Lett.* **2009,** *102*, 105901.

(S18) Volkov, A. N.; Zhigilei, L. V. Scaling Laws and Mesoscopic Modeling of Thermal Conductivity in Carbon Nanotube Materials. *Phys. Rev. Lett.* **2010,** *104*, 215902.

(S19) Yang, J. K.; Waltermire, S.; Chen, Y. F.; Zinn, A. A.; Xu, T. T.; Li, D. Y. Contact Thermal Resistance between Individual Multiwall Carbon Nanotubes. *Appl. Phys. Lett.* **2010,** *96*, 023109.

(S20) Evans, W. J.; Shen, M.; Keblinski, P. Inter-tube Thermal Conductance in Carbon Nanotubes Arrays and Bundles: Effects of Contact Area and Pressure. *Appl. Phys. Lett.* **2012,** *100*, 261908.
(S21) Deshpande, V. V.; Hsieh, S.; Bushmaker, A. W.; Bockrath, M.; Cronin, S. B. Spatially Resolved Temperature Measurements of Electrically Heated Carbon Nanotubes. *Phys. Rev. Lett.* **2009,** *102*, 105501.